Microstructure of selective laser melted AlSi10Mg alloy

Xihe Liu [a], Congcong Zhao [a,*], Xin Zhou [b], Zhijian Shen [a,c], Wei Liu [a,*]

[a] School of Materials Science and Engineering, Tsinghua University, Beijing 100084, China
[b] Science and Technology on Plasma Dynamics Lab, 710038 Xi'an, China
[c] Department of Materials and Environmental Chemistry, Arrhenius Laboratory, Stockholm University, S-106 91 Stockholm, Sweden

HIGHLIGHTS

- The nucleation at the border of melt pool and the columnar to equiaxed transition are responsible for the formation of equiaxed grains.
- Fine pseudoeutectic structure was observed in SLMed AlSi10Mg alloy because of the rapid solidification.
- The gradient microstructure is caused by the different temperature zones during the heating of laser beam.
- Coarse zones are formed by reheating the basic metal to semi-solid state when the temperature is at mushy zone.

GRAPHICAL ABSTRACT
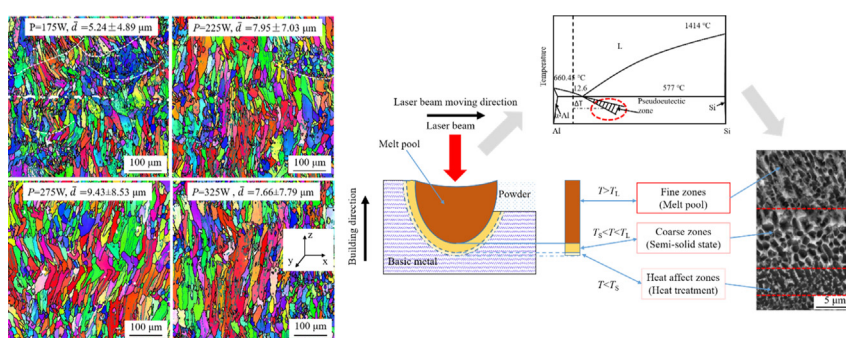
ARTICLE INFO

ABSTRACT

The influence of laser power during selective laser melting (SLM) on the grain morphology and texture component in AlSi10Mg alloy has been investigated, using electron backscattered diffraction (EBSD). Both equiaxed and columnar grains were observed. The formation of equiaxed grains was attributed to the huge thermal gradient on the border of melt pool and the columnar to equiaxed transition (CET) occurred in front of the columnar grains. The grain size of low laser power sample was found smaller than that of higher ones. A fine pseudoeutectic structure, in which Si existed as fibrous, was observed because of the high cooling rate. This paper, from a new angle, explained the formations of three different zones across the melt pool, which were differentiated by the morphology of Si phase. The three zones correspond to the three temperature zones, which were divided by liquidus and solidus temperature, during the heating by laser beam. The coarse zones are formed by reheating the basic metal to semi-solid state when the temperature is lower than the liquidus temperature but higher than the solidus temperature.

1. Introduction

As a kind of additive manufacturing (AM) technology, Selective Laser Melting (SLM) has attracted much interest in recent decades since it offers the possibility of producing complex geometries. Compared to traditional technologies, AM offers some distinct advantages such as short-time manufacture of complex and customized structures, high resolution and accuracy without almost any loss of material [1–3]. SLM is one of the powder bed based AM technologies. According to the sliced three-dimensional (3D) computer aided design (CAD) model, the metal products with complex freeform geometries are built by line-by-line and layer-by-layer laser scanning [4]. Several metals have been

* Corresponding authors.
   E-mail addresses: zhaocc819@mail.tsinghua.edu.cn (C. Zhao),
liuw@mail.tsinghua.edu.cn (W. Liu).

researched and produced using SLM, such as Ti-based alloys [5–7], Ni-based alloys [8–10], stainless steel [11–13], Al-based alloys [3,14,15].

Among Al-based alloys, AlSi10Mg alloy is a traditional cast alloy and highly demanded for many applications in aerospace and automotive because of its light weight, low thermal expansion and good mechanical properties [16,17]. AlSi10Mg alloy has good weldability because of the near eutectic composition of Al and Si. They are difficult to fabricate using traditional methods, however, due to the requirement of complex geometry [18,19]. Therefore, AlSi10Mg alloy is a good candidate for SLM. In order to fabricate dense AlSi10Mg alloy with good mechanical properties, the SLM parameters have been researched. Kempen et al. [20] affirmed a process parameter window zone between two liner boundaries in the P-v graph for optimal density through single track experiments. The influences of laser power and scanning speed on the surface morphologies of scan tracks for the samples with a single track and also bulk samples were investigated by Wei et al. [21]. The results showed that the porosity of the SLM-processed samples was significantly governed by energy density of laser beam and the hatch space. Furthermore, the unique microstructure caused by the rapid solidification and huge thermal gradients within the SLMed AlSi10Mg alloy was widely studies [22–24]. The microstructure of SLMed AlSi10Mg exhibited significant differences with as-cast ones. The primary α-Al matrix with cellular-dendritic microstructure and eutectic microstructure with very fine fibrous Si were reported [17,19,21–23]. The rapid solidification caused by SLM was responsible for the fine structure. Across the melt pool, three different zones were distinguished: fine zones, coarse zones, and heat affected zones (also called transitional zone in some reports). The reason for the formation of gradient microstructure has no uniform interpretation, especially for the coarse zones. Li et al. [17] conducted a systematically investigation on the influence of solution and artificial aging on the eutectic microstructure of SLMed AlSi10Mg alloy, which indicated that the eutectic Si was rejected from the supersaturated Al and Si particles were formed. Thijs et al. [22] investigated the fine microstructure and controllable texture of SLMed AlSi10Mg alloy with different scanning strategies. The change of thermal gradient G and growth rate R over the melt pool was considered as the reason for the change in the microstructure. ⟨100⟩ fiber along the scanning direction or a weak cubic texture preferentially around the building direction was found.

In this study, AlSi10Mg alloys are fabricated by SLM with different laser power. The grain morphology and texture within the SLMed AlSi10Mg on both longitudinal and transverse cross sections are investigated in details by using electron backscattered diffraction (EBSD). The reasons for the formation of equiaxed and columnar grains, which are observed on the longitudinal section, are discussed. Moreover, the fine microstructure in the grains is further investigated. This study provides new insights for the formation of eutectic Si phase and the different zones across the melt pool.

2. Material and methodology

2.1. Material

The AlSi10Mg powder used in this study, which was purchased from TLS Technik Company (Germany), had a nearly spherical morphology with a diameter of about 20–45 μm. The chemical composition is reported in Table 1. The powder was dried at 60 °C for 24 h to remove humidity and then sieved with a 74 μm sieve.

Table 1
Chemical compositions of AlSi10Mg powder (wt%).

Si	Mg	Mn	Cu	Fe	Ni	Zn	Sn	Al
9.2	0.48	0.21	0.26	0.84	0.17	0.25	0.11	Balance

Table 2
Parameters used for SLM processing.

Sample	P (W)	v (mm/s)	d (μm)	h (μm)	E (J/mm^3)
P1	175	300	50	150	77.8
P2	225	300	50	150	100
P3	275	300	50	150	122.2
P4	325	300	50	150	144.4

2.2. SLM process

The influence of the laser power on the grains orientation and crystal texture of AlSi10Mg alloy were taken into account, while other parameters were set as constant values. A TRUMPF Trumaform Lf250 machine was used to produce cubic samples with dimensions of 10 mm × 10 mm × 10 mm. Argon and Helium were used to prevent the oxidation in the working chamber. The parameters for all the samples (marked as P1, P2, P3, and P4) were listed in Table 2. The laser power was considered as the most influential parameter for the laser energy density (E), which was defined by the SLM processing parameters as shown in Eq. 1:

$$E = \frac{P}{v \times d \times h} \tag{1}$$

where P is the laser power, v is the laser scanning speed, d is the layer thickness and h is the hatch space.

Four different levels of laser power 175 W, 225 W, 275 W, and 325 W were selected to carry out in the SLM experiments, and the corresponding values of E were 77.8 J/mm^3, 100 J/mm^3, 122.2 J/mm^3, and 144.4 J/mm^3, respectively. The diameter of laser spot was 230 μm and the laser scanning strategy was strip exposure in which 67° rotation was used in each layer, as shown in Fig. 1. The island size was chosen to by 5×5 mm^2. 67° rotation was used in order to minimize the laser vector coincidence of adjacent layers and reduce the crystallographic texture.

2.3. Microscopic characterization

The microstructure of the SLMed samples were observed by optical microscope (OM, Nikon ECLIPSE LV100 TESCAN) and Scanning Electron Microscope (SEM, MIRA 3LMH). The different crystallographic orientations could be visualized by EBSD. The samples for OM observation was etched by Keller's solution (95 mL H$_2$O, 2.5 mL HNO$_3$, 1.5 mL HCl, and 1.0 mL HF). The samples for SEM observation (secondary electron imaging mode) were electrically polished with a solution of 5% nitric acid and 95% ethanol. The EBSD samples were polished using argon ion in a polishing instrument (Hitachi IM4000).
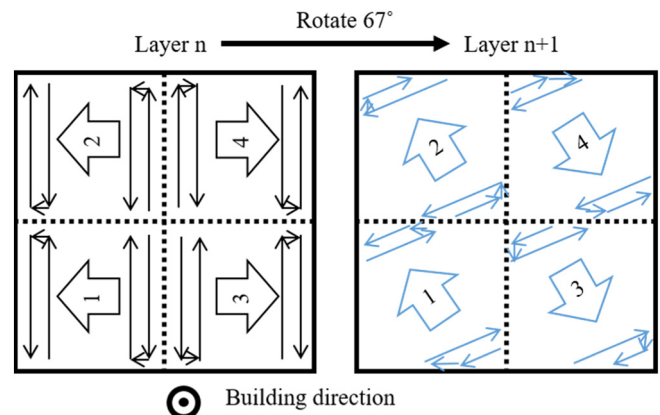

Fig. 1. The scanning strategy used for SLMed AlSi10Mg alloy.

3. Results

The Archimedes method was used to measure the relative density of SLMed samples with different laser power. The relative density of SLMed P1, P2, P3, and P4 are 97.51%, 98.04%, 97.81%, and 98.11%, respectively. It can be seen that the laser power and also the laser energy density used in this paper has no significant influence on the density of the fabricated samples.

3.1. The morphology of α-Al grains

With the consideration of 67° rotation in each layer during the building process, the microstructure has no significant difference between the xz-plane and yz-plane. Therefore, only longitudinal section and transverse cross section are cut from SLMed AlSi10Mg alloy, which represent xz-plane (or yz-plane) and xy-plane, respectively. Fig. 2 shows the results of inverse pole figure (IPF) orientation maps corresponding with grain boundaries obtained by EBSD for the SLMed AlSi10Mg alloy on the longitudinal section with different laser power. The EBSD analysis revealed that the microstructure is mainly composed of elongated grains, which are nearly perpendicular to the building direction (z direction in Fig. 2 (d)). Because of the growth of elongated grains towards the centre of the melt pool and the existence of small equiaxed grains, some of the melt pool boundary could be distinguished, as indicated by the dashed lines. In the vicinity of the melt pool boundary, small equiaxed grains appear. Grains are measured using a boundary misorientation angle definition of 2°. In order to reduce the influence of noise in the data, the crystallites of size less or equal to two map pixels are ignored. The microstructure characteristic statistics from the results of EBSD are listed in

Table 3
Summary of microstructural characteristics on longitudinal section for samples with different laser power.

Samples	P1	P2	P3	P4
Total grains (No.)	3723	2264	1474	1927
Mean diameter (μm)	7.39 ± 5.24	9.45 ± 7.12	11.90 ± 8.47	9.81 ± 8.19
Mean area (μm^2)	64.45 ± 122.29	109.94 ± 213.63	167.47 ± 260.95	128.18 ± 269.37
Max. area (μm^2)	2274.8	3321	3123	4504.5
f_{LAB}(%)	31.16	25.75	23.35	25.24

Table 3, in which the diameter is defined as the average equivalent circle diameter of each grain. With the consideration of inhomogeneous grain size, the fractions of grains in different ranges of area in the total area are used to describe the grain size distribution, as shown in Fig. 2(e). In the sample with the lowest laser power (P1), there are much more small grains (smaller than 50 μm^2) than other samples. Therefore, the average grain size of P1 is much smaller than that of others as a consequence of much more equiaxed grains. The large grains (larger than 500 μm^2) in P2, P3, and P4 are twice or three times more than that in P1. With the increase of laser power, the average grain size on the longitudinal section increases significantly. In the sample with the highest laser power (P4), however, the average grain size slightly decreases again. Although the average grain size of P4 is smaller than that of P3, the fraction of large grains (larger than 500 μm^2) is higher. Therefore, because of the simultaneous observation of elongated grains with large grain size and equiaxed grains with small size, it's hard to conclude that the grain size of P4 is smaller or not than that of P3. Considering the three-dimensional structure of grains, the morphology on transverse cross sections needs to be investigated.
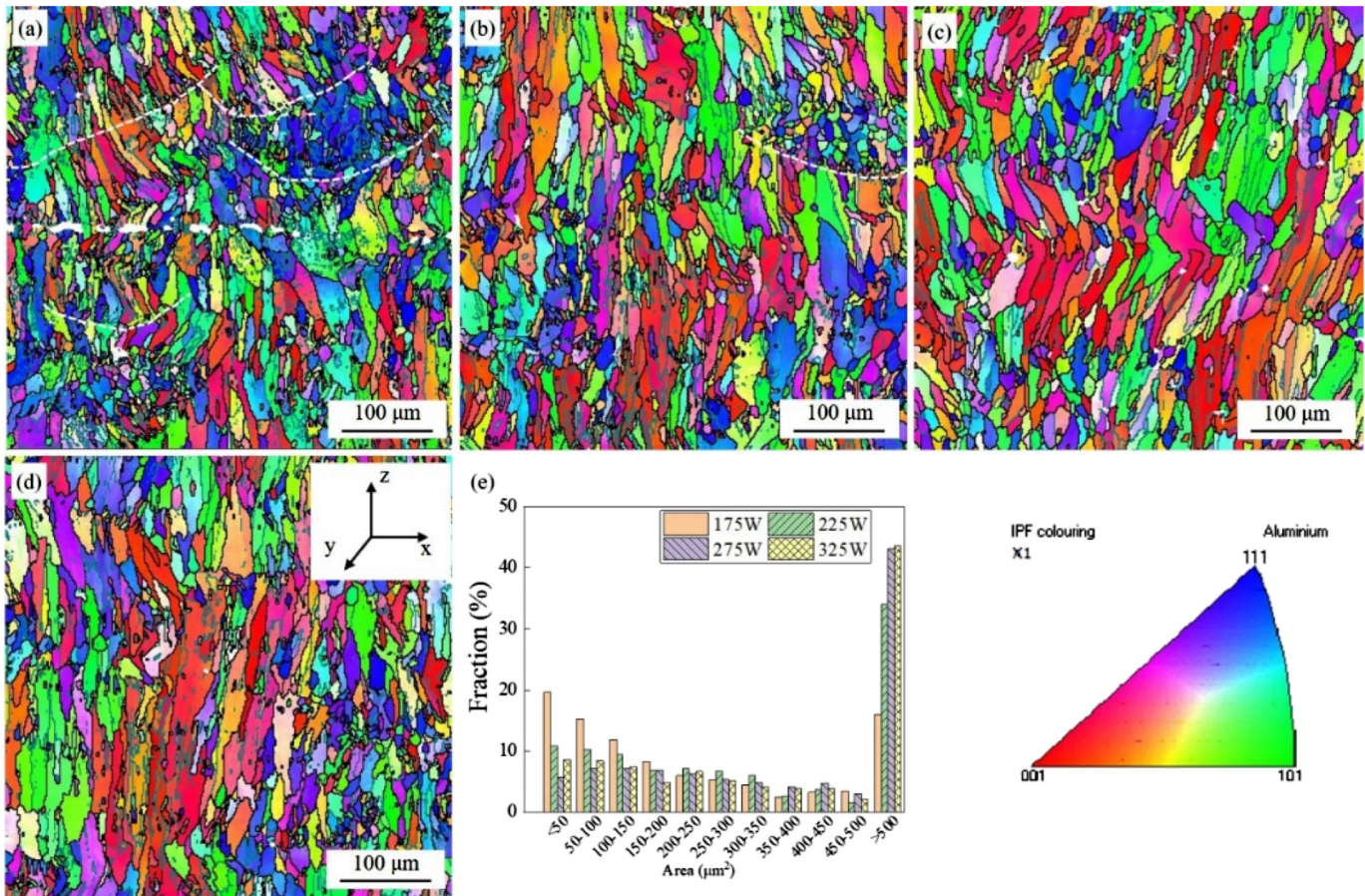

Fig. 2. EBSD inverse pole figure (IPF) orientation maps corresponding with grain boundaries on longitudinal section of SLMed AgSi10Mg alloy fabricated at $P = 175$ W (a), $P = 225$ W (b), $P = 275$ W (c), and $P = 325$ W (d). (e) Grain size distribution of the SLMed AlSi10Mg alloy with different laser power. The colour code representing the crystal orientation is given in the lower right corner.

Fig. 3 shows the IPF maps and grain size distribution of SLMed AlSi10Mg alloy on the transverse cross section with different laser power. Only equiaxed grains can be seen across the section. Similar with that on longitudinal section, some of melt pool boundary also can be distinguished because of the existence of small equiaxed grains. The microstructure characteristic statistics on the transverse cross section are shown in Table 4. The average grain size of P4 on transverse cross section is larger than that of P3, which is different from that on longitudinal section. It can be seen from the EBSD results on both of longitudinal and transverse cross sections, that the melt pools are composed of columnar grains and small equiaxed grains. The grain size in low laser power sample is much smaller than that in high laser power ones. The reason for the existence of both columnar and equiaxed grains and also the influence of laser power on the grain size will be discussed later.

The grain boundaries (the misorientation values higher than 2°) are also taken into consideration in the different laser power samples, as shown in Fig. 2 and Fig. 3. The misorientation values higher than 15° are marked by black lines and those lower than 15° are outlined by dark green lines. The fraction of low-angle boundaries (LABs, defined as boundaries with misorientation angle between 2° and 15°) in all of the samples is about 30% (the details are shown in Table 3 and Table 4). Fig. 4 indicates the misorientation angle distribution on both longitudinal and transverse cross sections of SLMed AlSi10Mg alloy with different laser power. The boundary misorientation distribution has no significant difference between the longitudinal section and transverse cross section, and also among different laser power. A peak located at a misorientation angle of 2–4° can be seen in all of the samples, which suggests the presence of high-density LABs within the columnar α-Al grains [25]. A fine substructure within the α-Al grains, which will be showed later, is responsible for the high-density LABs.

Table 4
Summary of microstructural characteristics on transverse cross section for samples with different laser power.

Samples	P1	P2	P3	P4
Total grains (No.)	5186	3795	4599	3666
Mean diameter (μm)	6.68 ± 3.81	7.70 ± 4.70	7.10 ± 4.06	7.90 ± 4.77
Mean area (μm²)	46.46 ± 63.34	63.86 ± 92.97	52.56 ± 71.07	66.95 ± 94.47
Max. area (μm²)	884.25	1638	1467	1262.3
f_{LAB}(%)	28.96	24.09	35.79	26.98

3.2. Crystallographic texture

On the transverse cross section, the small equiaxed grains around the melt pool boundary in Fig. 3 are presented with different colours, which shows a random crystallographic orientation. The majority of the grains, however, are coloured red (Fig. 3) when the orientation of the ⟨001⟩ directions is considered along scanning direction. Crystallographic textures in the grains are further analyzed by inverse pole figures along the scanning direction on both longitudinal and transverse cross sections, as shown in Fig. 5. The overall texture intensity of each sample is represented by the texture strength. In all samples, the inverse pole figures confirm the ⟨100⟩ fiber texture along the scanning direction. On the longitudinal section, the texture strength in P2 sample is higher than that of others. On the transverse cross section, the texture strength in P3 and P4 samples are almost three times higher than that in P1 and P2 samples. In short, the ⟨100⟩ fiber texture in high laser power samples are stronger than that in low laser power samples.

For cubic structure crystals, columnar cells prefer to grow in ⟨100⟩ direction. During the SLM process, some of the columnar grains grow
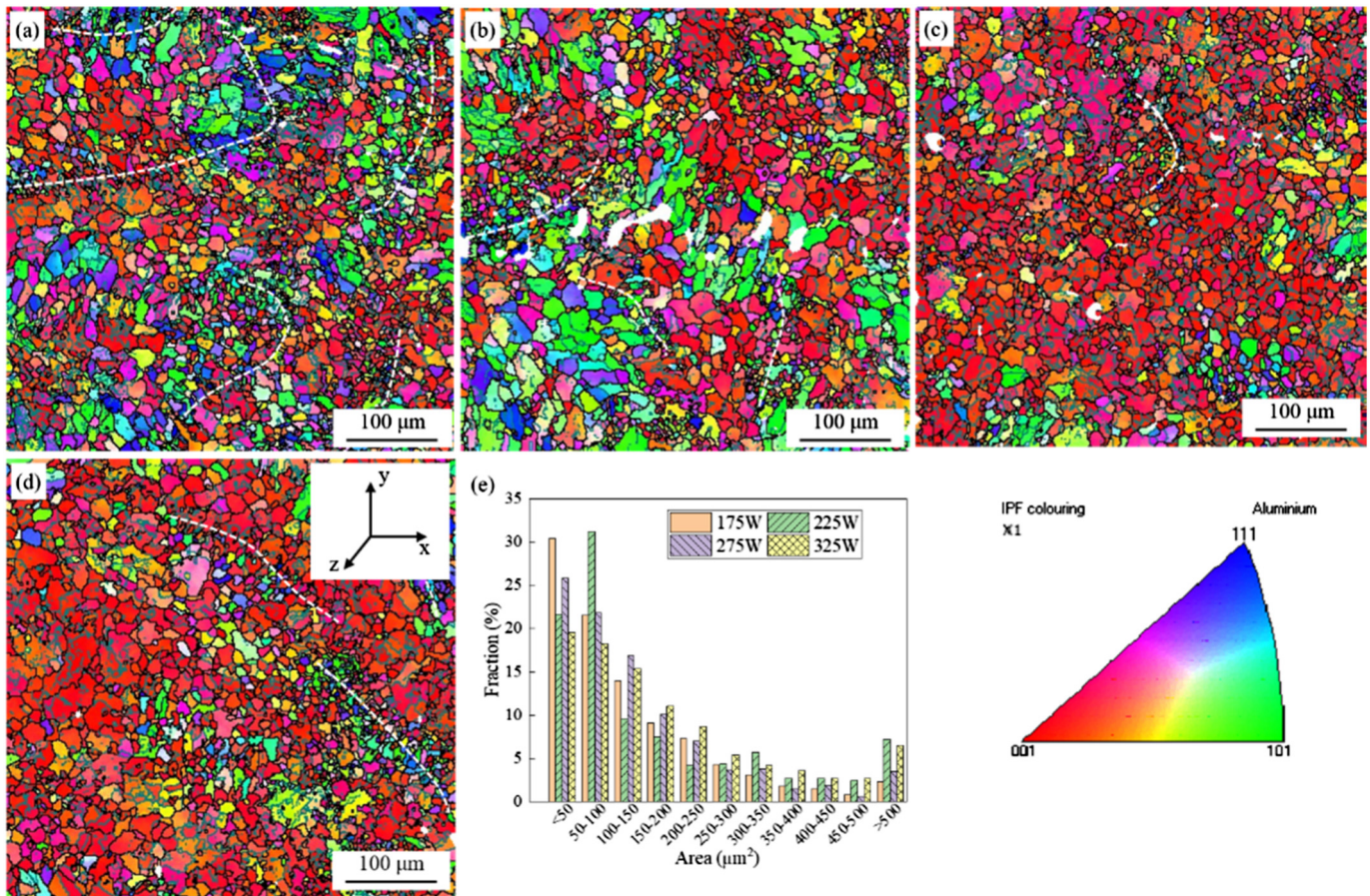

Fig. 3. IPF maps on transverse cross section of SLMed AgSi10Mg alloy fabricated at P = 175 W (a), P = 225 W (b), P = 275 W (c), and P = 325 W (d). (e) Grain size distribution of the SLMed AlSi10Mg alloy with different laser power. The colour code representing the crystal orientation is given in the lower right corner.
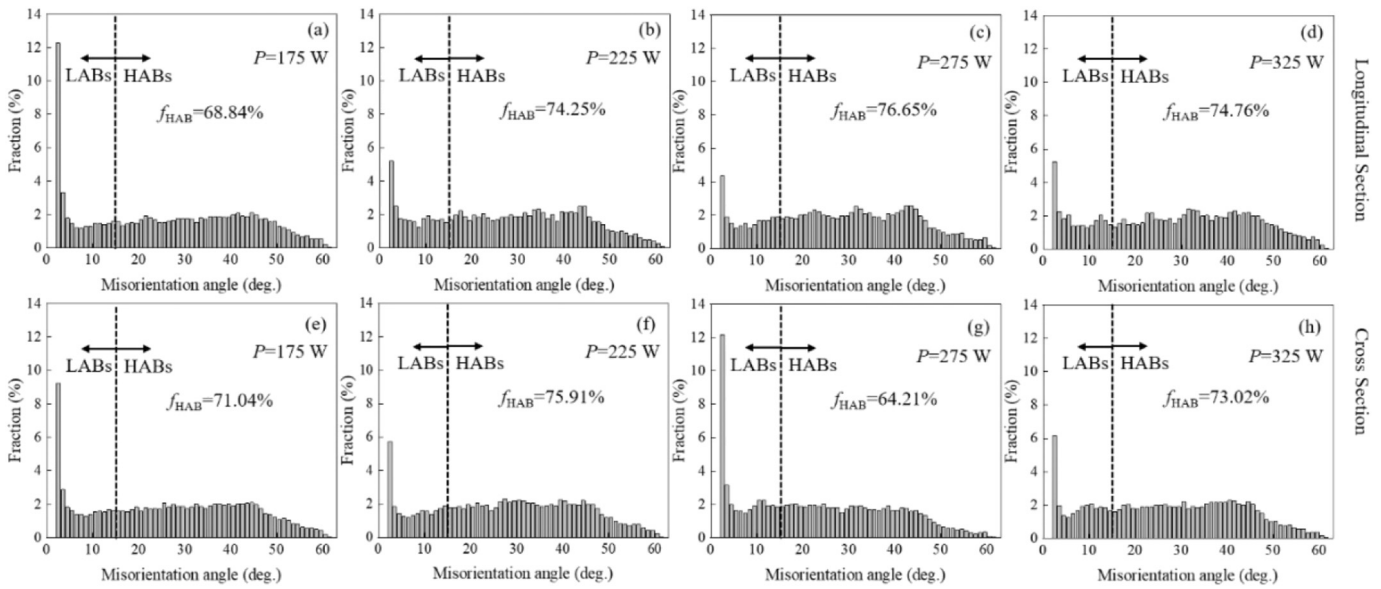
Fig. 4. Misorientation angle distribution on both longitudinal section (a-d) and transverse cross section (e-h) of SLMed AlSi10Mg alloy with different laser power. (a) and (e): $P = 175$ W, (b) and (f): $P = 225$ W, (c) and (g): $P = 275$ W, (d) and (h): $P = 325$ W.

epitaxially from the partly melted base metal, only if the heat flow is directed favorably to the $\langle 100 \rangle$ crystal direction of the substrate. Others formed because of the competitive growth with their $\langle 100 \rangle$ along the heat flow direction. This results in the $\langle 100 \rangle$ fiber texture along the scanning direction. In the samples with high laser power, the depth of remelted base metal is deeper than that in low laser power samples, which results in the dominant of epitaxial growth. This might be the reason for the higher texture intensity in high laser power samples.

3.3. The microstructure inside the grains

The morphology and texture of grains in SLMed AlSi10Mg alloy with different laser power were analyzed above from the EBSD results. A detailed microstructural characterization in the grains is further observed by the SEM images on the longitudinal and transverse cross sections of sample P4, as shown in Fig. 6. The melt pool track boundary can be seen obviously on both longitudinal and transverse cross sections. The reason for some discontinuous tracks is that the previously deposited layers have been remelted partially and heat transmission is not uniform, leading to the variations in depth and shape of the melt pool. A fine substructure composed of primary Al phase and nano-sized eutectic Al-Si network could be observed. The gray cellular-dendritic is Al and are decorated with white fibrous Si network. Inside the melt pool, cellular-dendrites grow towards the centre of the melt pool.

Across the melt pool, three zones could be differentiated from the morphology and size of the cellular-dendrites on both longitudinal and transverse cross sections.

(1) Fine zones: The fine zones account for the majority of the whole melt pool. The cellular-dendrites grow towards the center of the laser tracks. This is seen from difference between the transverse
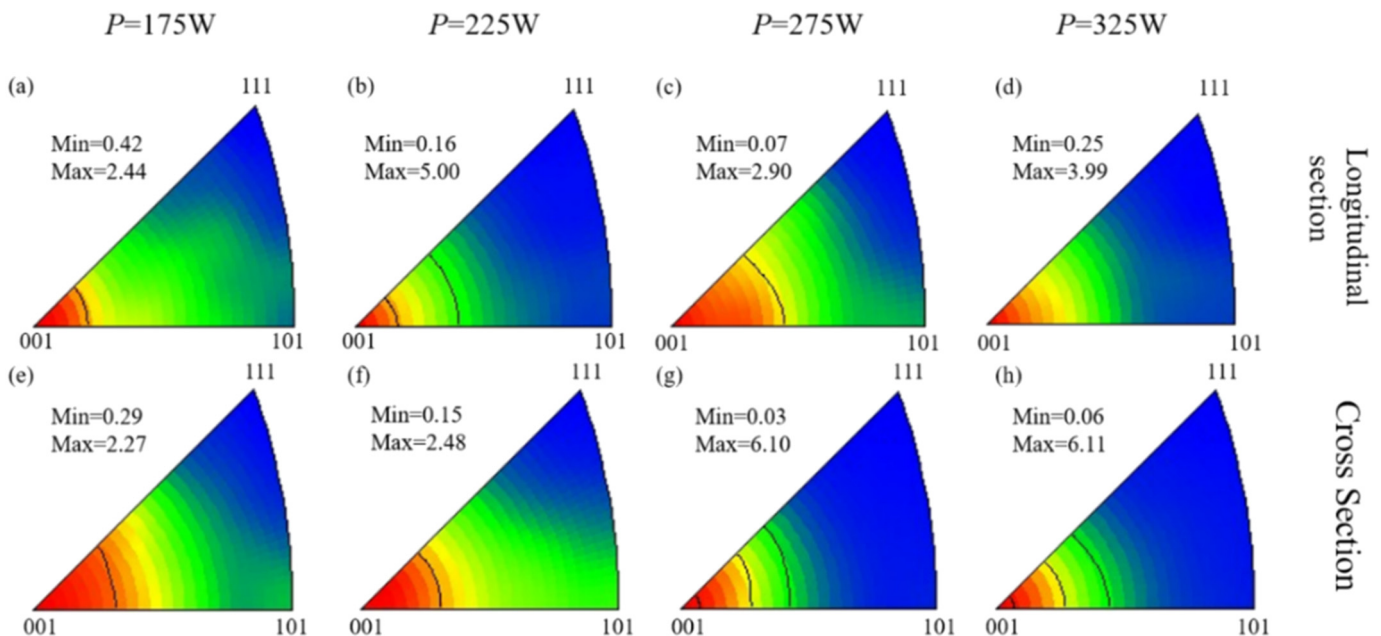

Fig. 5. Inverse pole figures parallel to the scanning direction on both longitudinal section (a-d) and transverse cross section (e-h) of SLMed AlSi10Mg alloy with different laser power. (a) and (e): $P = 175$ W, (b) and (f): $P = 225$ W, (c) and (g): $P = 275$ W, (d) and (h): $P = 325$ W.
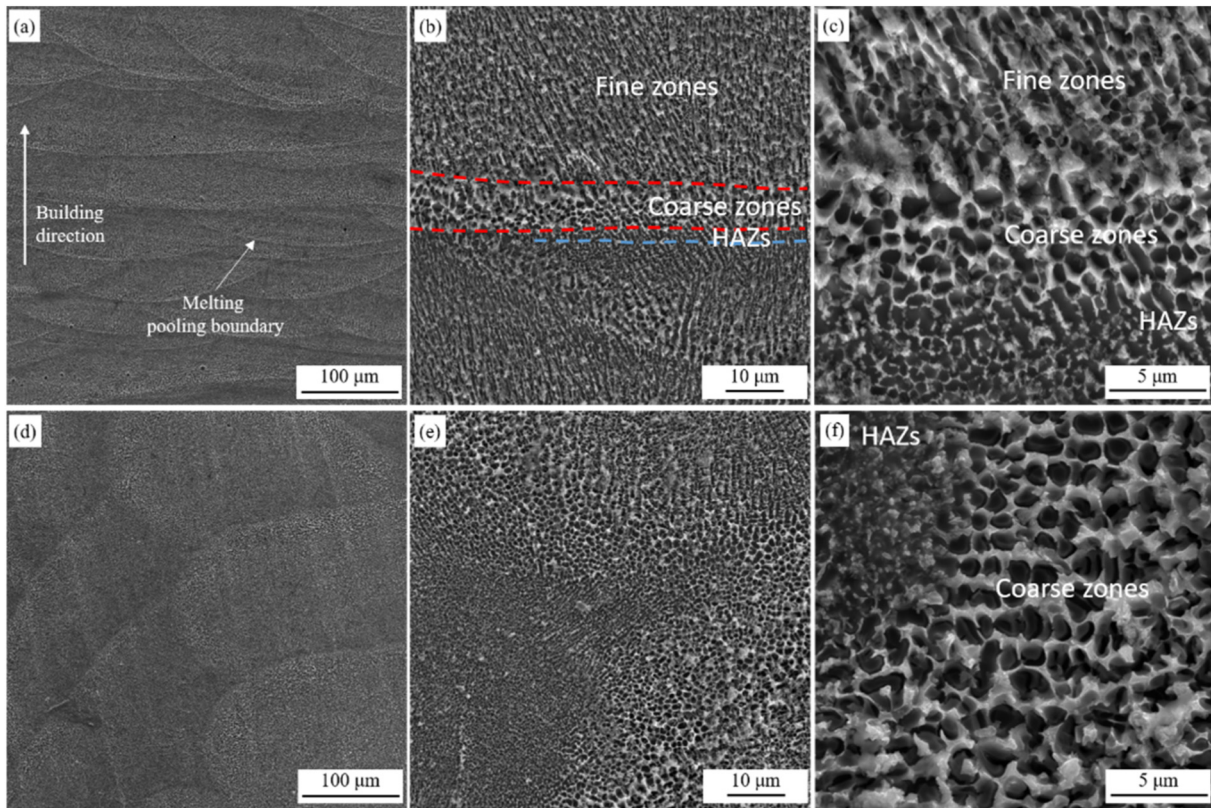
Fig. 6. The substructure in SLMed AlSi10Mg alloy on both longitudinal section (a, b, and c) and transverse cross section (d, e, and f).

cross section and longitudinal section. The width of Al cellular-dendrite is about 500 nm. From the edge to the center of the fine zones, the microstructure was gradually refined.

(2) Coarse zones: The coarse zones exist at the border of the melt pool. The width of the coarse zones is about 10 μm. The primary α-Al is equiaxed in the coarse zones (Fig. 6(c)), which is different with fine zones. No significant growth direction towards the center of the laser tracks is observed in the coarse zones. The length of α-Al is much smaller than that in fine zones. The width, however, is almost two times larger than that in fine zones.

(3) Heat affected zones (HAZs): A heat affected zone with about 2–3 μm in width can be seen right behind the coarse zones. In HAZs, the fibrous Si network was broken into particles, but the original network can still be traced. Moreover, some of the coarsen Si particles could also be seen in HAZs.

Take two melt pools from layer n and layer n + 1 for example, the order of the three different zones should be Fine zones-Coarse zones-HAZs-Fine zones. The details of the eutectic Al-Si network in the fine or coarse zones are showed in Fig. 7, which indicates that the Si phase displays a fibrous morphology. Similar results are also shown in previous reports [19,26]. The rapid solidification during the SLM process is responsible for the fibrous Si [27].
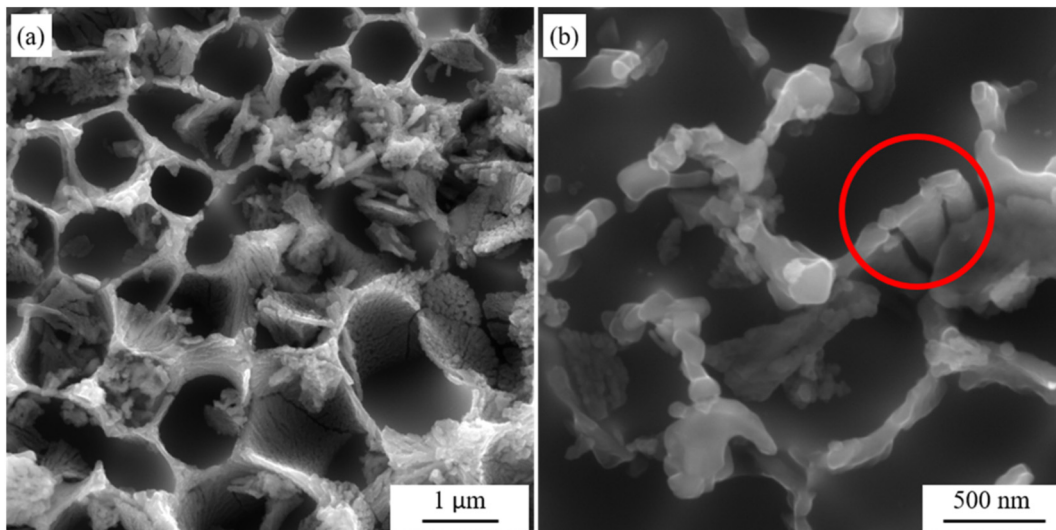

Fig. 7. (a) The fibrous Si network and (b) the fibrous morphology of Si phase.

4. Discussion

4.1. The influence of laser power on the grain size in SLMed AlSi10Mg alloy

It can be seen from the EBSD results on the longitudinal section and transverse cross section that the melt pools are composed of columnar grains and small equiaxed grains. The columnar grains, which tend to be elongated along the building direction, have a ⟨001⟩ fiber texture along the scanning direction. The equiaxed grains, however, have a random crystallographic orientation, which can be seen from the different colours in the IPF maps. The equiaxed grains could be observed at the border of melt pool and also other specific regions inside. In general, the solidification parameter G/R at the solid-liquid interface determines the solidification morphology, where G and R are the thermal gradient and solidification rate, respectively. Planar, cellular, columnar dendritic and equiaxed dendritic are formed in the sequence of decreasing values of G/R [22,28,29]. When the powder and part of base metal are melted by the laser, lots of small newly grains nucleate at the border of melt pool, because of the large value of G. Due to the high value of G/R, those newly nucleated grains competitively grow to columnar grains. Only a few grains with specific orientations, however, can grow further towards the center of melt pool. The texture results indicate that the grains with ⟨001⟩ orientation parallel to the scanning direction grow preferentially and form the columnar grains finally. Other grains remain as equiaxed grains at the border of melt pool. This is consistent with the result of texture, in which the equiaxed grains have a random crystallographic orientation. On the other hand, equiaxed grains could also form at the top of the melt pool, because of the columnar to equiaxed transition (CET). During the laser treatment, the CET might occur when the nucleation of sufficiently numerous equiaxed grains take place in the constitutionally undercooled liquid adjacent to the columnar dendritic front [30]. Due to the overlap between neighbouring tracks and the remelting of next layers, only a small part of the equiaxed grains formed by CET will be remained.

The fraction of equiaxed grains in the low laser power sample is significantly higher than that in high laser power samples. The most significant influence of different laser power on the solidification process would be the temperature in the melt pool. For a Gaussian distributed laser source, the maximum temperature of melt pool is proportional to the $\frac{P}{\sqrt{v}}$ ratio [7]:

$$T_{peak} \propto \frac{P}{\sqrt{v}} \qquad (2)$$

where P is power and v is scanning rate. With the same scanning rate, the temperature in the melt pool increases with the increasing laser power. In the sample with low laser power, the value of G is lower than that in high laser power samples for the lower peak temperature in the melt pool. As a consequence, G/R is small in low laser power sample, which results in the high fraction of equiaxed grains at the border of melt pool in sample P1. Moreover, with low laser power, the depth of melt pool is smaller than that in high laser power samples. This results in that more equiaxed grains at the top of melt pool might be remained in the finial sample.

4.2. The pseudoeutectic structure in SLMed AlSi10Mg alloy

AlSi10Mg alloy is approximately eutectic composition of Al-Si system (12.6 wt%). When compared to that of traditional casting, the SLMed material has a much finer eutectic structure. The volume fraction of primary α-Al phase is higher than that calculated by lever law according to the phase diagram of Al-Si. And also, the Si content in eutectic of SLMed AlSi10Mg alloy is much higher than the eutectic composition. The eutectic here is considered as a fine pseudoeutectic microstructure, which is due to the non-equilibrium solidification conditions. A large undercooling in front of the solid-liquid interface is achieved because of the high cooling rate during the SLM process. As the Al-Si belongs to a metal-nonmetal system, non-faceted interface of the α-Al grows more quickly than that of the faceted interface of the Si phase under the condition of large undercooling [31]. Therefore, the pseudoeutectic zone leans to the high Si region, as shown in Fig. 8. Zhang et al. [32] also reported a fine pseudoeutectic microstructure in Laser-cladded hypereutectic Ti-20%Si alloy, which was also caused by the high cooling rate. Moreover, the pseudoeutectic Al-Si structure was reported in spray formed Si-30%Al alloy [33]. Dinda et al. [34] indicated that the amount of primary Al increases with the increase of solidification velocity during the rapid solidification of eutectic or hypoertectic Al-Si alloy. The formation of pseudoeutectic structure is a good explanation for the large amount of primary Al phase and also the high composition of Si in eutectic structure.

4.3. The evaluation of microstructure across the melt pool

The unique microstructure of SLMed AlSi10Mg alloy is because of the high cooling rate (as high as 10^6 K/s) and thermal gradients during the SLM solidification process. As the result of high cooling rate, the α-Al phase shows an elongated dendritic morphology on the longitudinal section and a cellular morphology on the transverse cross section, which is surrounded with pseudoeutectic phase at the boundaries. The size of the microstructure is extremely fine because of the high thermal gradients.

For the formation of coarse zones at melt pool boundary, two possible reasons were mentioned in previous works. (i) The undercooling across the melt pool changed because of the Gauss distribution of the laser energy. The value of G reached the maximum at the centerline and the minimum at the boundary of the melt pool boundary. The value of $G \times R$, which determines the fineness of the structure, causes the formation of the coarse zones at the melt boundary [17,22,35,36]. But the change of $G \times R$ should be continuous across the melt pool, which cause a gradual change of the microstructure fineness. In SLMed AlSi10Mg alloy, however, the microstructure showed obvious demarcation between the coarse zones and the fine zones. The change of $G \times R$ across the melt pool could explain the gradually refined microstructure in the fine zones. (ii) Another explanation is that the size of the cellular at coarse zones grows continuously due to the remelting of solidified materials [21,37]. But the overlaps between the two layers should be much wider than that of observed coarse zones. In our opinion, the formation of coarse zones might be caused by the semi-solid state during the melting of next hatch or layer. This is similar with the thixo-route in semi-solid metal processing. During the thixo-route, the material is reheated to temperatures between solidus and liquidus (mushy zone) to generate a semi-solid structure, and finally the prepared feedstock is injected into the mold [38]. During the melting of
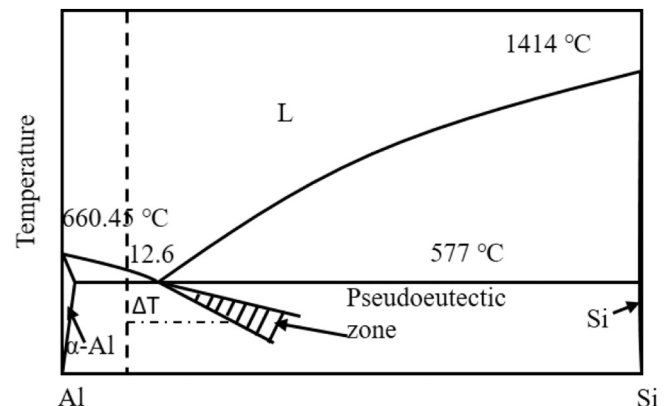

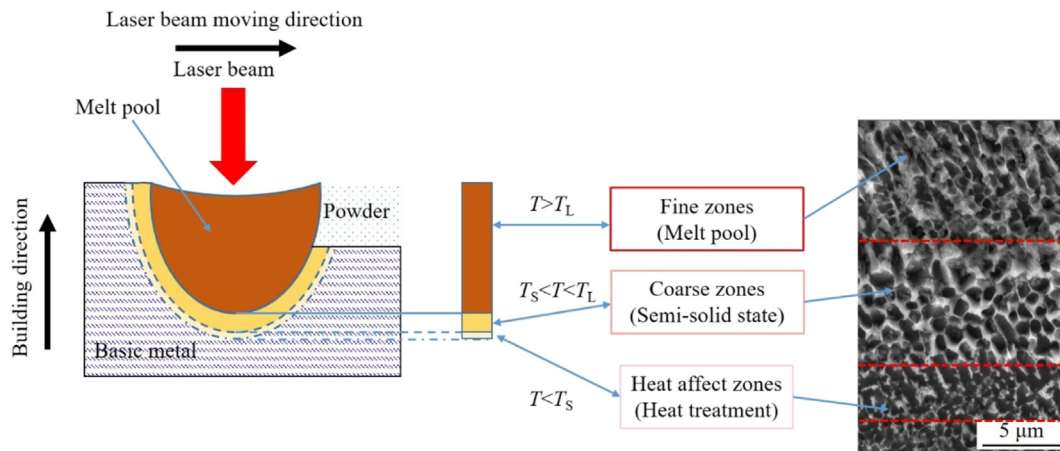**Fig. 8.** A diagram of pseudoeutectic zone in Al-Si alloy.

Fig. 9. Schematic diagram for the formation of three zones observed in SLMed AlSi10Mg. T_L is the liquidus temperature, T_S is the solidus temperature.

next hatch or layer, the temperature decreases from the contact point of laser to the basic metal. When the temperature is higher than liquidus, the powder or basic metal is melted to liquid and then solidified, which is the fine zones in the finial alloy. When the temperature is lower than liquidus but higher than solidus, the basic metal is reheated to semi-solid state, corresponding with the coarse zones. The semi-solid processed Al-Si alloys have been researched by many experts, because of the wide solidification range. The dendrite primary α-Al phase changes to globular morphology after the semi-solid metal process with high swirling intensity [39,40]. The dendrite primary Al become rounder with 12 Hz vibration (the average particle velocity above the frequency of 12 Hz was estimated to be 60–150 mm/s). The fluid flow mechanism of the SLM process was investigated in many reports. Yuan et al. [41] indicated that the liquid material flow was mainly dominated by the Marangoni convection, which was induced by the temperature difference and the attendant surface tension gradient. Wang et al. [42] stated that the maximum velocity vector of the Marangoni flow on the cross-section of the melt pool can reach to 2.34 m/s. It can be seen that the velocity of Marangoni flow caused by laser is much higher than that in 12 Hz vibration. As a consequence, the cellular-dendrite was broke and equiaxed primary α-Al was formed when the basic metal was remelted to semi-solid state during the melting of next hatch or layer. The dendrite space in fine zones is very small because of the lack of secondary dendrite. The primary branches are coarsened when the basic metal (original fine zones in the previous hatch or layer) is reheated to semi-solid state. This is consistent with the observation in previous literature [43].

In the HAZs, the temperature is lower than solidus, and the basic metal wasn't melted at all by the laser beam. But the heat source acts as a heat treatment for the basic metal. Because of the high moving speed of the laser and the high cooling rate, the time for the basic metal to maintain a high temperature is extremely short. Consequently, the microstructure of Si cells changes only in very small regions (presents as HAZs), which is affected by the high temperature in an instant. The α-Al contents extend the solid solubility of Si because of the high cooling rate. Because of the heat treatment in the HAZs, Si precipitates from the supersaturated Al. Si particles form and grow, and finally the Si cells' boundary disappears. Similar results, in which Si cells change to Si particles, could be seen in other reports about the heat treatment of SLMed AlSi10Mg alloy [17,25,44]. The schematic diagram of the corresponding relationship between the temperature and microstructure in different zones is shown in Fig. 9.

5. Conclusions

1. Both equiaxed and columnar grains were observed in the SLMed AlSi10Mg alloy. The large value of G at the melting boundary and

CET in front of the columnar grains was responsible for the formation of equiaxed grains.

2. The grain size in low laser power sample is much smaller than that in higher ones. The fraction of equiaxed grains in low laser power sample is higher than that in higher ones because of the lower G/R value.
3. The fine pseudoeutectic structure was observed in SLMed AlSi10Mg alloy. The Si phase in the pseudoeutectic structure is observed as fibours because of the rapid solidification.
4. The three zones observed from the microstructure are caused by the three temperature zones during the heating of laser beam. (i) When the temperature is higher than the liquidus temperature, the powder and overlap are melted and then solidified as cellular-dendrites. Show up as fine zones in the finial microstructure. (ii) When the temperature is lower than the liquidus temperature but higher than the solidus temperature, the basic metal is reheated to semi-solid state, in which the primary α-Al phase changes to globular morphology. Show up as coarse zones. (iii) When the temperature is lower than the solidus temperature, the heat source acts as a heat treatment for the basic metal and causes the formation and growth of Si particles. Show up as HAZs.

CRediT authorship contribution statement

Xihe Liu: Validation, Formal analysis, Investigation, Writing - original draft. **Congcong Zhao:** Validation, Formal analysis, Writing - original draft, Writing - review & editing. **Xin Zhou:** Investigation. **Zhijian Shen:** Conceptualization, Supervision, Project administration. **Wei Liu:** Conceptualization, Methodology, Supervision, Project administration, Funding acquisition.

Acknowledgements

References

[1] W.E. Frazier, Metal additive manufacturing: a review, J. Mater. Eng. Perform. 23 (2014) 1917–1928, https://doi.org/10.1007/s11665-014-0958-z.
[2] D. Buchbinder, W. Meiners, K. Wissenbach, R. Poprawe, Selective laser melting of aluminum die-cast alloy—correlations between process parameters, solidification conditions, and resulting mechanical properties, J. Laser Appl. 27 (2015) S29205. https://doi.org/10.2351/1.4906389.
[3] H. Rao, S. Giet, K. Yang, X. Wu, C.H.J. Davies, The influence of processing parameters on aluminium alloy A357 manufactured by Selective Laser Melting, Mater. Des. 109 (2016) 334–346, https://doi.org/10.1016/j.matdes.2016.07.009.

[4] J. Suryawanshi, K.G. Prashanth, U. Ramamurty, Tensile, fracture, and fatigue crack growth properties of a 3D printed maraging steel through selective laser melting, J. Alloys Compd. 725 (2017) 355–364, https://doi.org/10.1016/j.jallcom.2017.07.177.

[5] L. Thijs, F. Verhaeghe, T. Craeghs, J. Van Humbeeck, J.P. Kruth, A study of the microstructural evolution during selective laser melting of Ti-6Al-4V, Acta Mater. 58 (2010) 3303–3312, https://doi.org/10.1016/j.actamat.2010.02.004.

[6] T. Ishimoto, K. Hagihara, K. Hisamoto, S.H. Sun, T. Nakano, Crystallographic texture control of beta-type Ti–15Mo–5Zr–3Al alloy by selective laser melting for the development of novel implants with a biocompatible low Young's modulus, Scr. Mater. 132 (2017) 34–38, https://doi.org/10.1016/j.scriptamat.2016.12.038.

[7] S. Cao, Z. Chen, C.V.S. Lim, K. Yang, Q. Jia, T. Jarvis, D. Tomus, X. Wu, Defect, microstructure, and mechanical property of Ti-6Al-4V alloy fabricated by high-power selective laser melting, Jom. 69 (2017) 2684–2692, https://doi.org/10.1007/s11837-017-2581-6.

[8] F. Geiger, K. Kunze, T. Etter, Tailoring the texture of IN738LC processed by selective laser melting (SLM) by specific scanning strategies, Mater. Sci. Eng. A 661 (2016) 240–246, https://doi.org/10.1016/j.msea.2016.03.036.

[9] S.H. Sun, K. Hagihara, T. Nakano, Effect of scanning strategy on texture formation in Ni-25 at.%Mo alloys fabricated by selective laser melting, Mater. Des. 140 (2018) 307–316, https://doi.org/10.1016/j.matdes.2017.11.060.

[10] K. Kunze, T. Etter, J. Grässlin, V. Shklover, Texture, anisotropy in microstructure and mechanical properties of IN738LC alloy processed by selective laser melting (SLM), Mater. Sci. Eng. A 620 (2014) 213–222, https://doi.org/10.1016/j.msea.2014.10.003.

[11] M. Ma, Z. Wang, X. Zeng, A comparison on metallurgical behaviors of 316L stainless steel by selective laser melting and laser cladding deposition, Mater. Sci. Eng. A 685 (2017) 265–273, https://doi.org/10.1016/j.msea.2016.12.112.

[12] Z. Sun, X. Tan, S.B. Tor, W.Y. Yeong, Selective laser melting of stainless steel 316L with low porosity and high build rates, Mater. Des. 104 (2016) 197–204, https://doi.org/10.1016/j.matdes.2016.05.035.

[13] D. Wang, C. Song, Y. Yang, Y. Bai, Investigation of crystal growth mechanism during selective laser melting and mechanical property characterization of 316L stainless steel parts, Mater. Des. 100 (2016) 291–299, https://doi.org/10.1016/j.matdes.2016.03.111.

[14] J. Wu, X.Q. Wang, W. Wang, M.M. Attallah, M.H. Loretto, Microstructure and strength of selectively laser melted AlSi10Mg, Acta Mater. 117 (2016) 311–320, https://doi.org/10.1016/j.actamat.2016.07.012.

[15] A. Aversa, M. Lorusso, G. Cattano, D. Manfredi, F. Calignano, E.P. Ambrosio, S. Biamino, P. Fino, M. Lombardi, M. Pavese, A study of the microstructure and the mechanical properties of an Al-Si-Ni alloy produced via selective laser melting, J. Alloys Compd. 695 (2017) 1470–1478, https://doi.org/10.1016/j.jallcom.2016.10.285.

[16] N. Read, W. Wang, K. Essa, M.M. Attallah, Selective laser melting of AlSi10Mg alloy: process optimisation and mechanical properties development, Mater. Des. 65 (2015) 417–424, https://doi.org/10.1016/j.matdes.2014.09.044.

[17] W. Li, S. Li, J. Liu, A. Zhang, Y. Zhou, Q. Wei, C. Yan, Y. Shi, Effect of heat treatment on AlSi10Mg alloy fabricated by selective laser melting: microstructure evolution, mechanical properties and fracture mechanism, Mater. Sci. Eng. A 663 (2016) 116–125, https://doi.org/10.1016/j.msea.2016.03.088.

[18] U. Tradowsky, J. White, R.M. Ward, N. Read, W. Reimers, M.M. Attallah, Selective laser melting of AlSi10Mg: influence of post-processing on the microstructural and tensile properties development, Mater. Des. 105 (2016) 212–222, https://doi.org/10.1016/j.matdes.2016.05.066.

[19] X. Ding, L. Wang, Heat transfer and fluid flow of molten pool during selective laser melting of AlSi10Mg powder: simulation and experiment, J. Manuf. Process. 26 (2017) 280–289, https://doi.org/10.1016/j.jmapro.2017.02.009.

[20] K. Kempen, L. Thijs, J. Van Humbeeck, J.P. Kruth, Processing AlSi10Mg by selective laser melting: parameter optimisation and material characterisation, Mater. Sci. Technol. 31 (2015) 917–923, https://doi.org/10.1179/1743284714Y.0000000702.

[21] P. Wei, Z. Wei, Z. Chen, J. Du, Y. He, J. Li, Y. Zhou, The AlSi10Mg samples produced by selective laser melting: single track, densification, microstructure and mechanical behavior, Appl. Surf. Sci. 408 (2017) 38–50, https://doi.org/10.1016/j.apsusc.2017.02.215.

[22] L. Thijs, K. Kempen, J.P. Kruth, J. Van Humbeeck, Fine-structured aluminium products with controllable texture by selective laser melting of pre-alloyed AlSi10Mg powder, Acta Mater. 61 (2013) 1809–1819, https://doi.org/10.1016/j.actamat.2012.11.052.

[23] L.P. Lam, D.Q. Zhang, Z.H. Liu, C.K. Chua, Phase analysis and microstructure characterisation of AlSi10Mg parts produced by Selective Laser Melting, Virtual Phys. Prototyp. 10 (2015) 207–215, https://doi.org/10.1080/17452759.2015.1110868.

[24] Y.J. Liu, Z. Liu, Y. Jiang, G.W. Wang, Y. Yang, L.C. Zhang, Gradient in microstructure and mechanical property of selective laser melted AlSi10Mg, J. Alloys Compd. 735 (2018) 1414–1421, https://doi.org/10.1016/j.jallcom.2017.11.020.

[25] N. Takata, H. Kodaira, K. Sekizawa, A. Suzuki, M. Kobashi, Change in microstructure of selectively laser melted AlSi10Mg alloy with heat treatments, Mater. Sci. Eng. A 704 (2017) 218–228, https://doi.org/10.1016/j.msea.2017.08.029.

[26] S. Marola, D. Manfredi, G. Fiore, M.G. Poletti, M. Lombardi, P. Fino, L. Battezzati, A comparison of selective laser melting with bulk rapid solidification of AlSi10Mg alloy, J. Alloys Compd. 742 (2018) 271–279, https://doi.org/10.1016/j.jallcom.2018.01.309.

[27] M. Pierantoni, M. Gremaud, P. Magnin, D. Stoll, W. Kurz, The coupled zone of rapidly solidified Al-Si alloys in laser treatment, Acta Metall. Mater. 40 (1992) 1637–1644, https://doi.org/10.1016/0956-7151(92)90106-O.

[28] J. Liu, A.C. To, Quantitative texture prediction of epitaxial columnar grains in additive manufacturing using selective laser melting, Addit. Manuf. 16 (2017) 58–64, https://doi.org/10.1016/j.addma.2017.05.005.

[29] H.L. Wei, J.W. Elmer, T. Debroy, Origin of grain orientation during solidification of an aluminum alloy, Acta Mater. 115 (2016) 123–131, https://doi.org/10.1016/j.actamat.2016.05.057.

[30] M. Gäumann, C. Bezençon, P. Canalis, W. Kurz, Single-crystal laser deposition of superalloys: processing-microstructure maps, Acta Mater. 49 (2001) 1051–1062, https://doi.org/10.1016/S1359-6454(00)00367-0.

[31] D.M. Herlach, Non-equilibrium solidification of undercooled metallic melts, Key Eng. Mater. 81-83 (1993) 83–94, https://doi.org/10.4028/www.scientific.net/KEM.81-83.83.

[32] H. Zhang, Z. Zhang, T.M. Yue, The pseudo-eutectic microstructure and enhanced properties in laser-cladded hypereutectic Ti–20%Si coatings, Metals. 7 (2017) 33, https://doi.org/10.3390/met7020033.

[33] Y. Wei, B. Xiong, Y.A. Zhang, H.W. Liu, F. Wang, B.H. Zhu, Microstructures variation of spray formed Si-30%Al alloy during densification process, Trans. Nonferrous Metals Soc. China 16 (S3) (2006) 1570–1573.

[34] G.P. Dinda, A.K. Dasgupta, J. Mazumder, Evolution of microstructure in laser deposited Al-11.28%Si alloy, Surf. Coat. Technol. 206 (2012) 2152–2160, https://doi.org/10.1016/j.surfcoat.2011.09.051.

[35] F. Trevisan, F. Calignano, M. Lorusso, J. Pakkanen, A. Aversa, E.P. Ambrosio, M. Lombardi, P. Fino, D. Manfredi, On the selective laser melting (SLM) of the AlSi10Mg alloy: process, microstructure, and mechanical properties, Materials. 10 (2017) https://doi.org/10.3390/ma10010076.

[36] C. Yan, L. Hao, A. Hussein, P. Young, J. Huang, W. Zhu, Microstructure and mechanical properties of aluminium alloy cellular lattice structures manufactured by direct metal laser sintering, Mater. Sci. Eng. A 628 (2015) 238–246, https://doi.org/10.1016/j.msea.2015.01.063.

[37] J. Zou, Y. Zhu, M. Pan, T. Xie, X. Chen, H. Yang, A study on cavitation erosion behavior of AlSi10Mg fabricated by selective laser melting (SLM), Wear. 376–377 (2017) 496–506, https://doi.org/10.1016/j.wear.2016.11.031.

[38] S. Nafisi, D. Emadi, M.T. Shehata, R. Ghomashchi, Effects of electromagnetic stirring and superheat on the microstructural characteristics of Al-Si-Fe alloy, Mater. Sci. Eng. A 432 (2006) 71–83, https://doi.org/10.1016/j.msea.2006.05.076.

[39] J.W. Zhao, S.S. Wu, L.Z. Xie, P. An, Y.W. Mao, Effects of vibration and grain refiner on microstructure of semisolid slurry of hypoeutectic Al-Si alloy, Trans. Nonferrous Met. Soc. China. 18 (2008) 842–846, https://doi.org/10.1016/S1003-6326(08)60146-6.

[40] O. Lashkari, R. Ghomashchi, Rheological behavior of semi-solid Al-Si alloys: effect of morphology, Mater. Sci. Eng. A 454–455 (2007) 30–36, https://doi.org/10.1016/j.msea.2007.01.003.

[41] P.P. Yuan, D.D. Gu, D.H. Dai, Particulate migration behavior and its mechanism during selective laser melting of TiC reinforced Al matrix nanocomposites, Mater. Des. 82(2015) 46–55. doi:https://doi.org/10.1016/j.matdes.2015.05.041.

[42] D. Wang, C.H. Song, Y.Q. Yang, Y.C. Bai, Investigation of crystal growth mechanism during selective laser melting and mechanical property characterization of 316L stainless steel parts, Mater. Des. 100 (2016) 291–299, https://doi.org/10.1016/j.matdes.2016.03.111.

[43] E.J. Zoqui, M.T. Shehata, M. Paes, V. Kao, E. Es-Sadiqi, Morphological evolution of SSM A356 during partial remelting, Mater. Sci. Eng. A 325 (2002) 38–53, https://doi.org/10.1016/S0921-5093(01)01401-0.

[44] K.G. Prashanth, S. Scudino, H.J. Klauss, K.B. Surreddi, L. Löber, Z. Wang, A.K. Chaubey, U. Kühn, J. Eckert, Microstructure and mechanical properties of Al-12Si produced by selective laser melting: effect of heat treatment, Mater. Sci. Eng. A 590 (2014) 153–160, https://doi.org/10.1016/j.msea.2013.10.023.